

## Article

# Alternatives to Improve Performance and Operation of a Hybrid Solar Thermal Power Plant Using Hybrid Closed Brayton Cycle

Faustino Moreno-Gamboa<sup>1</sup>, Ana Escudero-Atehortua<sup>2</sup> and César Nieto-Londoño<sup>2,\*</sup> 

<sup>1</sup> Grupo de Investigación FLUTER, Engineering School, Universidad Francisco de Paula Santander, Cucuta 540004, Colombia; faustinomoreno@ufps.edu.co

<sup>2</sup> Engineering School, Universidad Pontificia Bolivariana, Medellin 050031, Colombia; ana.escudero@upb.edu.co

\* Correspondence: cesar.nieto@upb.edu.co

**Abstract:** Hybrid solar thermal power plants using the Brayton cycle are currently of great interest as they have proven to be technically feasible. This study evaluates mechanisms to reduce fuel consumption and increase the power generated, improving plant efficiency. An energy and exergy model for the hybrid solar plant is developed using an estimation model for the solar resource to determine the plant operation under specific environmental conditions. The effect of using different working fluids in the Brayton cycle, such as air, and helium in transcritical conditions and carbon dioxide in subcritical and supercritical conditions, is evaluated. Additionally, the plant's exergy destruction and exergy efficiency are evaluated. In those, it can be highlighted that the helium cycle in the same operating conditions compared to other working fluids can increase the power by 160%, increasing fuel consumption by more than 390%.



check for updates

**Citation:** Moreno-Gamboa, F.; Escudero-Atehortua, A.; Nieto-Londoño, C. Alternatives to Improve Performance and Operation of a Hybrid Solar Thermal Power Plant Using Hybrid Closed Brayton Cycle. *Sustainability* **2022**, *14*, 9479. <https://doi.org/10.3390/su14159479>

Academic Editors: Kumar Patchigolla, Chris Sansom and Peter Turner

Received: 10 June 2022

Accepted: 11 July 2022

Published: 2 August 2022

**Publisher's Note:** MDPI stays neutral with regard to jurisdictional claims in published maps and institutional affiliations.



**Copyright:** © 2022 by the authors. Licensee MDPI, Basel, Switzerland. This article is an open access article distributed under the terms and conditions of the Creative Commons Attribution (CC BY) license (<https://creativecommons.org/licenses/by/4.0/>).

**Keywords:** Brayton cycle; concentrated solar power; hybrid solar thermal power plant hybrid; exergy analysis; working fluid selection

## 1. Introduction

The growing demand for sustainable and efficient energy generation to reduce the environmental impact is an issue of great concern. In this sense, solar thermal cycles are an excellent alternative to be used where the solar resource is sufficient. One of these cycles is the solar thermal Brayton cycle. This cycle can be highly viable when its efficiency, emissions, assembly, and operating costs are considered, according to a comparison made by Chen et al. [1], and also contributes to accomplishing some Sustainable Development Goals (SDGs) [2].

Gas turbine cycles are typically open cycles that operate with air as the working fluid and are suitable for locations with low water availability [3]. However, closed gas turbine cycles allow different working fluids and alternative heat sources such as concentrating solar systems, biomass, or nuclear reactors to be used [4,5]. According to Olumayegun et al. [6], the main advantages of closed Brayton cycles are that, unlike the open cycle, it can use solid fuels such as coal and biomass as well as solar, nuclear, and waste heat. Additionally, using different working fluids with favourable thermal properties (e.g., helium, nitrogen, carbon dioxide, argon, neon, and gas mixtures) can also avoid fouling and corrosion.

At first, the closed Brayton cycle using air as a working fluid and having the heat source from fossil fuels seems to outperform open cycles [6]. However, efforts have been made in order to improve open cycle performance, using low emission systems [7] or studying high-temperature heat exchangers, using liquid or solid fuels, and searching for high temperatures at the turbine inlet [8,9]. Nuclear energy is another possible heat source for a closed Brayton cycle, including mobile power generation [10]. On the other hand, using biomass in external combustion chambers for gas turbines reduces GHG emissions and could be obtained from waste in many urban and rural areas. In addition,

the combustion chamber can be a vertical gasifier [11]. In other cases, biomass has been used to increase the turbine inlet temperature operating in a combined cycle to increase net power [12]. Other studies show that pre-drying biomass with fuel moisture content ranging from 50% to 80% can improve the efficiency by more than 10% [13], proving that biomass drying can have a significant impact on the heat released and gas turbine working fluid conditioning, especially when doing the initial heating [14].

Another promising energy source for closed-cycle gas turbine systems is concentrating solar power (CSP) plants, which can deliver clean, renewable thermal energy even at turbine inlet temperatures above 1300 K [15]. Studies have been based on solar concentration systems, with a central tower and a heliostat field with hybridization systems to regulate the operation for changes or the absence of a solar resource. Prototypes with up to 70% solar contribution have been studied [16]. In addition, some cycle improvements have been considered to increase its efficiency [17,18]. Other works have focused on the development of thermodynamic models that allow an energy analysis of hybrid solar thermal plants operating in Brayton cycles and the evaluation of the net power and efficiency [19,20], as well as the evaluation of operating temperatures and fuel consumption [21–23].

Concerning working fluids, the air has been the typical fluid used in gas turbines, but given the current need to improve the efficiency, alternative working fluids are being sought to make significant advances in the operation of these systems. In this sense, carbon dioxide presents itself as a promising option, especially in supercritical conditions (i.e., above  $P_c = 7.3773$  MPa and  $T_c = 304.12$  K). Supercritical carbon dioxide ( $SCO_2$ ) has the advantages of being non-toxic, non-corrosive, and non-flammable. Additionally, given its high density near the critical point, it allows more compact turbomachinery and heat exchangers, significantly reducing the compressor's work [24]. Conventional recuperators for Brayton cycles have been evaluated within the  $SCO_2$  cycle, in which special care is taken to avoid pinch point formation due to the high specific heat of the fluid at high pressure and compared to a recompression cycle [25]. Additionally, the  $SCO_2$  cycle configurations with pre-compression have been studied, achieving efficiencies higher than 45% and found optimal operating conditions at the compressor inlet of 305 K and 7.7 MPa, with a pressure ratio of 2.6 [26]. On the other hand, it has been demonstrated that  $SCO_2$  cycles can be technically feasible and present overall efficiencies over 50%. Mechanisms continue to be pursued to improve this efficiency using bottoming cycles, as is the case of transcritical bottoming cycles of carbon dioxide, which determine a decrease in the levelized energy cost when there is a turbine entry temperature increase [27,28]. Organic cycles have also been included, considering several working fluids and improving efficiencies by up to 11% [29,30].

Another fluid that is expected to be helpful in closed systems is helium, whose main characteristic is that its specific heat at constant pressure is approximately four times greater than that of air, implying that enthalpy and temperature changes are more significant [31,32]. One of the first experiences reported with helium was a closed-cycle gas turbine used to drive a cryogenic facility for gas liquefaction without power generation outside the facility [33]. Then, in 1974, a power plant was installed that used blast furnace gas as fuel and allowed the application of helium at high temperatures and on a large scale, followed by another closed-cycle helium gas-turbine test facility [34]. Recently, a combined gas turbine cycle with external combustion and a lower steam cycle was developed, where the cooling gas in the primary system was helium and a mixture of helium and nitrogen for the secondary system [35]. It is estimated that the advantages of helium as a working fluid can be beneficial not only in power cycles; even the possibility of using it in closed cycles for propulsion purposes is being studied, achieving better performance at a low scale [36]. Regarding the use of helium in Brayton cycles, it can represent essential advantages such as high efficiency [37], good heat transfer coefficients, and lower pressure losses [6], which favors the use of solar concentration systems [38].

This paper is structured as follows: Section 2 describes the models used, starting with the solar radiation model that allows an hourly irradiation distribution based on monthly

average daily values. Next, a thermodynamic model of a hybrid solar plant of a closed Brayton cycle is developed, where the irreversibilities in the processes of compression, expansion, and heat transfer are considered. Finally, the exergy destruction models for the different components of the system are presented. Section 3 describes the conditions of the working fluids used in this study. Section 4 shows the plant simulation for the Colombian conditions, including evaluating the thermal efficiency at maximum conditions and power as a function of the pressure ratio for each working fluid. The simulation and search for an optimum operation point are performed in the same section. Finally, Section 4 presents the conclusions regarding the models and analysis developed and the specific operating conditions in Colombia.

## 2. Materials and Methods

This section describes the models for solar resource evaluation. In addition, the schematic of the Brayton cycle solar thermal plant and its respective description are presented together with the plant's thermodynamic model for the energy and the exergy destruction analysis.

### 2.1. Solar Model

Among the hourly solar radiation models, the daily integration model developed by Gueymard [39,40] was initially designed to predict monthly hourly average global irradiance and was validated with data from 135 meteorological stations. This model is considered the most accurate after being compared and verified against others already developed and validated [41,42]. In the daily integration model, the total irradiance on a horizontal surface  $I_h$  is defined as the sum of its components, the direct radiation  $I_{bh}$  and the diffuse  $I_{dh}$ ; as a result, direct radiation is defined as follows:

$$I_{bh} = I_h - I_{dh}. \quad (1)$$

The time-of-day relationships for diffuse  $r_d$  and global  $r_{tg}$  radiation are introduced below:

$$r_d = I_{dh}/\bar{D}_h, \quad (2)$$

$$r_{tg} = I_h/\bar{H}_h, \quad (3)$$

where  $\bar{D}_h$  and  $\bar{H}_h$  represent the long-term monthly daily average for total and diffuse radiation, obtained from the National Aeronautics and Space Administration (NASA) [43]. These data are calculated with information from 22 years of analysis. The direct radiation as a function of the hour-day ratios and global and diffuse radiation is expressed as follows:

$$I_{bh} = r_{tg}\bar{H}_h - r_d\bar{D}_h, \quad (4)$$

where the ratio  $r_d$  is obtained according to the following equation [43]:

$$r_d = (\pi/T)(\cos \omega - \cos \omega_s)/(\sin \omega_s - \omega_s \cos \omega_s), \quad (5)$$

where  $\omega_s$  is the sunrise angle for a given day and  $\omega$  is the hourly angle over the same day. These values are estimated according to the literature [44]. On the other hand, the average daily extraterrestrial radiation on a horizontal surface,  $H_o$ , can be estimated as

$$H_o = (24/\pi)\omega_s RE_{sc} \sin h_o, \quad (6)$$

where  $R = (D_o/D)^2$  is the mean distance between the sun and the earth correction factor,  $D$  is the distance between the sun and the earth, which varies according to the location of the earth in the elliptical orbit around the sun,  $D_o$  is the mean annual distance between the

sun and the earth, estimated to be  $1.496 \times 10^{11}$  m. This correction factor can be estimated using the following equations:

$$R = 1.00011 + 0.034221 \cos x + 0.00128 \sin x + 0.000719 \cos 2x + 0.000077 \sin x, \quad (7)$$

$$x = 360(n - 1)/365.242 \quad (8)$$

In addition,  $h_o$  represents the mean daily solar elevation outside the atmosphere and is estimated with the following equations:

$$\sin h_o = qA(\omega_s)/\omega_s, \quad (9)$$

$$q = \cos L \cos \delta, \quad (10)$$

$$A(\omega_s) = \omega_s \sin \omega_s - \omega_s \cos \omega_s, \quad (11)$$

where  $L$  is the latitude of the location where the solar resource will be estimated, and  $\delta$  is the declination calculated according to [44]. In addition, the mean brightness index  $K_t$  and the sunshine duration  $S_o$  per day are introduced using the following equations:

$$K_t = \bar{H}_h/H_o, \quad (12)$$

$$S_o = (24/\pi)\omega_s. \quad (13)$$

The relationship between the horizontal hourly radiation and the total horizontal daily radiation is established by the factor  $r_{tg}$ , is obtained as follows:

$$r_{tg} = r_d((1 + q(a_2/a_1)A(\omega_s)r_d(24/\pi))/(1 + q(a_2/a_1)B(\omega_s)/A(\omega_s))), \quad (14)$$

where  $a_2$  takes the more excellent value between 0.054 and the calculated using least-squares adjustments. The values of  $a_1$  and  $a_2$  are estimated as follows:

$$a_1 = 0.41342K_t + 0.61197K_t^2 - 0.01886K_tS_o + 0.00759S_o, \quad (15)$$

$$a_2 = 0.28116 + 2.24p75K_t - 1.7611K_t^2 - 1.84535 \sin h_o + 1.681 \sin^3 h_o, \quad (16)$$

and  $B(\omega_s)$  being obtained from

$$B(\omega_s) = \omega_s(0.5 + \cos^2 \omega_s) - 0.75(\sin(2\omega_s)). \quad (17)$$

The verification and validation using the DI model were carried out with the value of direct solar radiation in Seville, Spain. The model results are compared with the measured values for a particular day using the Mean Absolute Bias Error (MABE) and the Root Mean Square Error (RMSE), finding 0.2010 and 0.2266, respectively. The results show that the DI model has been adequately implemented; the validation details can be found [45].

## 2.2. Schematic and Energy Model of Hybrid Solar Thermal Plant

The thermodynamic analysis of the solar thermal plant carried out in this work is based on the schematic in Figure 1. In this, the configuration of a closed-cycle hybrid concentrating solar thermal power plant operating is shown; it is composed of a compressor (process 1–2) and a turbine, both considered under adiabatic and irreversible conditions. Then, a recuperator or regenerator takes advantage of the working fluid temperature at the turbine outlet to increase the air of the fluid that comes at the compressor outlet (process 2–3), where the heat transfer process is isobaric. Next is the solar receiver (process 3–4), which receives the concentrated irradiation from the heliostat field and delivers heat to the working fluid through a heat exchanger. Subsequently, the combustion chamber (process 4–5) burns natural gas and releases heat into the working fluid using a heat exchanger. Finally, the working fluid enters the turbine (process 5–6), generating the system power. After the regenerator, a heat exchanger (process 1–6) regulates the inlet temperature of the compressor.

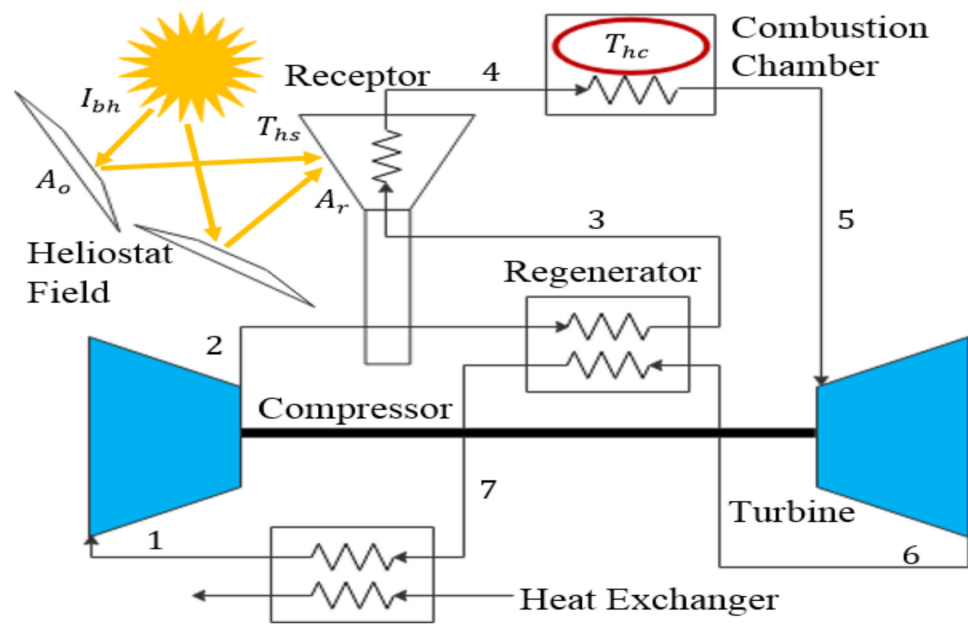


Figure 1. Schematic diagram of the hybrid solar thermal power plant.

Figure 2 shows the temperature–entropy diagram representing the whole cycle of the solar thermal plant. In this figure,  $\dot{Q}_{hs}$  is the heat supplied by the solar concentrating system (process 3–4),  $\dot{Q}_{hc}$  is the heat supplied by the combustion chamber heat exchanger (process 4–5) and  $\dot{Q}_h$  is the waste heat released by the system to the environment with temperature  $T_0$  (process 7–1). Additionally, the pressure drop  $\Delta p_s$  in the heat supply (process 2–5) and  $\Delta p_i$  for heat rejection (process 6–1) are considered.

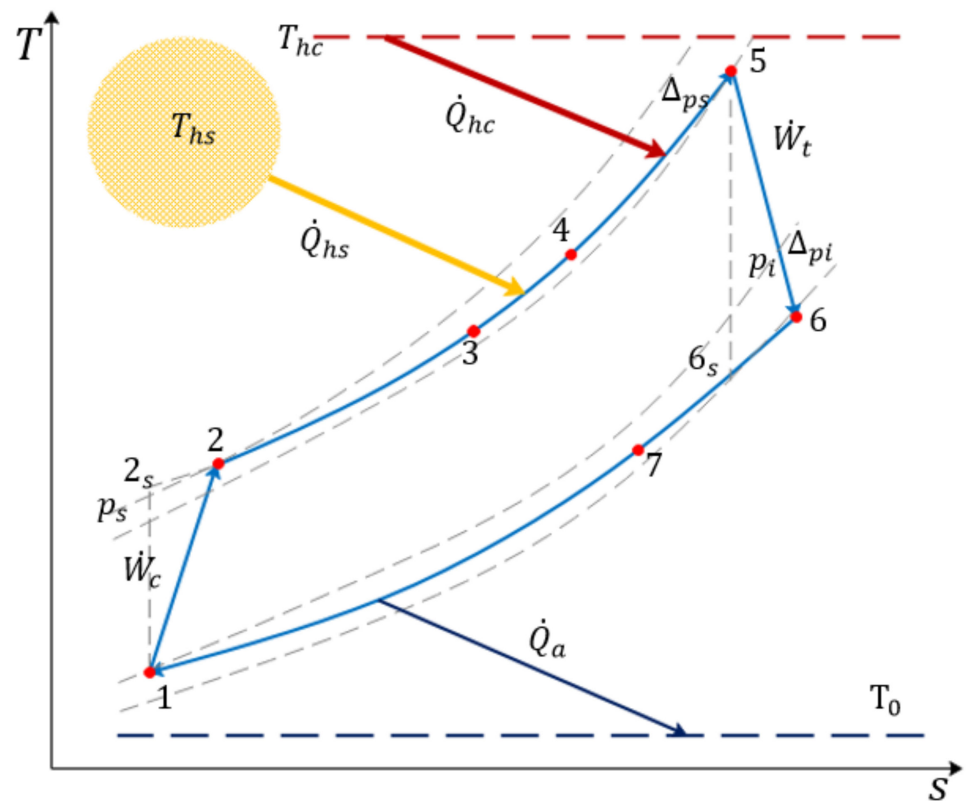


Figure 2. Plant temperature vs. entropy diagram.

According to the system diagram, the energy balance in the compressor can be expressed as

$$\dot{W}_c = \dot{m}(h_2 - h_1), \quad (18)$$

where  $\dot{W}_c$  is the compressor work. The overall cycle pressure ratio  $r_p$  and the pressure ratio for the compressor  $r_c$ , are defined as

$$r_c = r_p = \frac{P_{2s}}{P_1} \quad (19)$$

In Equation (18),  $\dot{m}$  is the working fluid mass flow, and  $h$  is the enthalpy in each defined state. Finally, the isentropic compressor efficiency can be expressed as

$$\eta_c = (h_{2s} - h_1) / (h_2 - h_1), \quad (20)$$

The regenerator supplies heat to the working fluid leaving the compressor from the energy available in it at the turbine outlet, only if the inequality  $T_6 > T_2$  is satisfied and is related by the regenerator efficiency as follows:

$$\eta_r = (h_7 - h_6) / (h_2 - h_6) = (h_3 - h_2) / (h_6 - h_2), \quad (21)$$

The energy balance and isentropic efficiency  $\eta_t$  of the turbine are presented below, where  $\dot{W}_t$  is the work of the turbine and  $r_t$  is the pressure ratio for the turbine.

$$\dot{W}_t = \dot{m}(h_6 - h_5), \quad (22)$$

$$r_t = (D_{ps} D_{pi} r_p) = P_5 / P_{6s}, \quad (23)$$

$$\eta_t = (h_6 - h_5) / (h_{6s} - h_5), \quad (24)$$

Finally, pressure losses occur in the heat transfer processes associated with each equipment (processes 2–5 and 6–1); consequently, the lines in Figure 2 are not continuous. As a result, and in order to evaluate the pressure losses analytically, overall loss coefficients  $D_{ps}$  in the heat supply process (process 2–5) and  $D_{pi}$  in the heat exhaust process (process 6–1) are defined, as shown in Figure 2. These coefficients are defined as follows [32,33]:

$$D_{ps} = (P_s - \Delta_{ps}) / P_s, \quad (25)$$

$$D_{pi} = (P_i - \Delta_{pi}) / P_i, \quad (26)$$

where  $P_s$  and  $P_i$  are the upper and lower pressure of the cycle, and  $\Delta_p$  is the pressure drops according to Figure 2. Therefore, the pressure losses in the heat addition and extraction processes are considered at the turbine inlet and outlet.

After passing through the compressor, the working fluid receives three heat additions. The first of these occurs in the regenerator, as explained above; the second one occurs in the solar concentrating system, in which solar radiation is initially received by the heliostat field, which reflects heat  $\dot{Q}_r$ , evaluated as

$$\dot{Q}_r = \eta_0 A_o I_{bh}. \quad (27)$$

This heat reaches the central tower receiver, where heat loss,  $\dot{Q}_p$ , occurs.  $\dot{Q}_{hst}$  is the heat available in the receiver, which is estimated as

$$\dot{Q}_{hst} = \dot{Q}_r - \dot{Q}_p. \quad (28)$$

In Equation (27),  $\eta_0$  is the optical efficiency of the heliostat field, which depends on aspects such as the cosine efficiency losses, surface quality, cleanliness, tracking system, and reflectivity, among others. Since this work's objective is not to estimate this efficiency,

the overall efficiency of the heliostat field reported in the literature will be used [46]. On the other hand, the heat losses in the receiver  $\dot{Q}_p$  can be evaluated by assigning linear values for the temperature difference regarding convection and conduction losses and nonlinear values for radiation losses [47]. In this case, the analysis is performed according to the definition of losses in the central receiver as follows:

$$\dot{Q}_p = A_r \left( h_w (T_{hs} - T_0) + U_{cond} (T_{hs} - T_0) + \alpha \sigma (T_{hs}^4 - T_0^4) \right) \quad (29)$$

where  $T_{hs}$  is the temperature of the central receiver,  $h_w$  and  $U_{cond}$  are the convective and conductive heat transfer coefficients, respectively,  $\alpha$  is the emissivity of the surface of the central receiver,  $\sigma$  is the Stefan-Boltzmann constant and  $A_r$  is the receiver area. In the above equation, a conduction and convection heat transfer coefficient  $U_l$  can be included, thus expressing  $\dot{Q}_p$  as

$$\dot{Q}_p = A_r \left( U_l (T_{hs} - T_0) + \alpha \sigma (T_{hs}^4 - T_0^4) \right). \quad (30)$$

The receiver delivers heat,  $\dot{Q}_{hs}$ , to the working fluid (process 3–4), through a heat exchanger with efficiency  $\eta_{is}$  [21,48]; both are defined as follows:

$$\eta_{is} = (T_4 - T_3) / (T_{hs} - T_3), \quad (31)$$

$$\dot{Q}_{hs} = \eta_{is} \dot{Q}_{hst} = \dot{m} (h_4 - h_3). \quad (32)$$

The above expressions allow the solar concentration system efficiency to be evaluated as follows:

$$\eta_s = \left( \dot{Q}_r - \dot{Q}_p \right) / (I_{bh} A_o). \quad (33)$$

Replacing values in Equation (33) and solving  $\eta_s$  gives

$$\eta_s = \eta_0 - \frac{U_l (T_{hs} - T_0)}{I_{bh} (A_o / A_r)} - \frac{\alpha \sigma (T_{hs}^4 - T_0^4)}{I_{bh} (A_o / A_r)}. \quad (34)$$

The third and final process of heat delivery to the working fluid (process 4–5) occurs in the combustion chamber, which can be evaluated as

$$\dot{Q}_{hct} = \eta_{cc} Q_{lhv} \dot{m}_f, \quad (35)$$

where  $\dot{Q}_{hct}$  is the heat available in the chamber,  $\eta_{cc}$  is the combustion chamber efficiency,  $Q_{lhv}$  is the lower heating value of the fuel and  $\dot{m}_f$  is the fuel mass flow rate. Similarly, as in the receiver, heat is delivered to the working fluid, as

$$\dot{Q}_{hc} = \varepsilon_{ic} \dot{Q}_{hct} = \dot{m} (h_5 - h_4), \quad (36)$$

using a heat exchanger with effectivity  $\varepsilon_{ic}$  [21,48], defined as

$$\varepsilon_{ic} = (T_5 - T_4) / (T_{hc} - T_4). \quad (37)$$

On the other hand, the values of  $\dot{Q}_{hs}$  and  $\dot{Q}_{hc}$  represent the external heat delivered to the working fluid by the solar concentrating system and the combustion chamber. Therefore,  $\dot{Q}_h$ , is defined as the total heat delivered to the working fluid expressed as

$$\dot{Q}_h = \dot{Q}_{hc} + \dot{Q}_{hs} = \dot{m} (h_5 - h_3). \quad (38)$$

The definition of the heat input makes it possible to determine the solar factor, which is the fraction of the solar heat received by the working fluid,

$$f = \dot{Q}_{hs} / \dot{Q}_h = \dot{Q}_{hs} / (\dot{Q}_{hc} + \dot{Q}_{hs}). \quad (39)$$

Additionally, the cycle transfers heat to the environment,  $\dot{Q}_a$ ,

$$\dot{Q}_a = \dot{m}(h_7 - h_1), \quad (40)$$

with an efficiency  $\eta_l$  [21,22],

$$\eta_l = (T_1 - T_7) / (T_0 - T_7). \quad (41)$$

The overall power cycle efficiency,  $\eta_h$ , and the net power output of the solar thermal plant,  $P$ , are evaluated as follows:

$$P = \dot{W}_t - \dot{W}_c = \dot{Q}_h - \dot{Q}_a, \quad (42)$$

$$\eta_h = (\dot{W}_t - \dot{W}_c) / (\dot{m}_f Q_{lhv} + I_{bh} A_o), \quad (43)$$

Finally, the fuel conversion rate of the plant is defined as the power generated over the energy of the fuel consumed [22],

$$r_e = P / (\dot{m}_f Q_{lhv}). \quad (44)$$

The fuel conversion rate considers fuel consumption and its effect on operating costs. The plant's solar and thermodynamic resource models are implemented in Modelica language; for the validation of the thermodynamic model, the Solugas experimental plant and the analysis presented by M Santos et al. [22] have been used. As a result, the proposed model reaches errors in global efficiency of 0.66%, for the solar fraction of 4.1%, outlet solar concentrator temperature of 1.5% and fuel consumption of 2.4%. The parameters and details of the validation are presented in [45].

### 2.3. Hybrid Solar Thermal Plant Exergy Model

This section depicts the exergy model, for which the exergy balance of each component is performed. Exergy destruction has been estimated for each component of hybrid central tower and heliostat field concentrating solar thermal power plants [49]. In addition, the energy and exergy study of a solar plant with helium and an organic lower cycle [50] and the exergy analysis of a hybrid supercritical carbon dioxide central tower solar plant for different locations in Saudi Arabia [51] have also been carried out. Finally, exergy models have been developed for Brayton plants with different heat sources, including fossil fuel burning and using renewable energy sources [52].

In the development of this model, it is assumed that the kinetic and potential exergy changes are neglected, as well as the chemical exergy of the components and the general exergy balance equation are reduced for a single steady flow system [31]. The equations for the exergy destruction of the components such as the compressor (45), turbine (46), and recuperator (47) are described below. In addition, as the cycle dissipates heat to the environment, the exergy destruction is evaluated with Equation (48).

$$\dot{E}_{d,c} = \dot{m}((h_1 - h_2) - T_0(s_1 - s_2)) + \dot{W}_c, \quad (45)$$

$$\dot{E}_{d,t} = \dot{m}((h_5 - h_6) - T_0(s_5 - s_6)) - \dot{W}_t, \quad (46)$$

$$\dot{E}_{d,r} = \dot{m}((h_6 - h_7 + h_2 - h_3) - T_0(s_6 - s_7 + s_2 - s_3)), \quad (47)$$

$$\dot{E}_{d,a} = \dot{m}((h_7 - h_1) - T_0(s_1 - s_2)). \quad (48)$$

Additionally, it is required to estimate the exergy destruction in the combustion chamber. For this purpose, the analysis of the exergy balance in a control volume containing the combustion chamber and its heat exchanger is simplified. In this volume, the flows of the working fluid  $\dot{m}$  and the fuel  $\dot{m}_f$  are defined as inputs and the combustion product gases as outputs ( $\dot{m}_a + \dot{m}_f$ ). Additionally, the working fluid from the receiver enters state 4 and exits state 5.

Then, the exergy balance in the combustion chamber is

$$\dot{E}_{d,cc} = \dot{m}_a E_{m,a} + \dot{m}_f E_{m,f} - (\dot{m}_a + \dot{m}_f) E_{m,g} + \dot{m}((h_4 - h_5) - T_0(s_4 - s_5)), \quad (49)$$

where  $E_{m,a}$ ,  $E_{m,f}$  and  $E_{m,g}$  are the working fluid, fuel, and exhaust gases specific exergies, respectively. The above specific exergy values are estimated from a relationship for mixtures described as  $E_m = E_q/PM_m$  [46], where  $PM_m$  is the molar mass of the mixture and  $E_q$  is the chemical exergy of the natural gas, working fluid, or combustion products, which are estimated by the following expression:

$$E_q = \sum_{i=1}^j y_i E_i + R_g T_0 \sum_{i=1}^j y_i \ln(y_i), \quad (50)$$

where  $y_i$  is the fraction of each fuel component,  $E_i$  the specific exergy of the fuel component, and  $R_g$  the universal gas constant. Therefore, it is possible to determine the exergy of the combustion chamber exit gases, fuel, and the working fluid entering the combustion chamber.

For the concentrating solar power system, the total solar energy input to the system is defined based on the maximum available work as a function of the solar radiation, according to [53,54],

$$\dot{E}_{x,s} = I_{bh} A_o \left[ 1 + \frac{1}{3} \left( \frac{T_0}{T_s} \right)^4 - \frac{4}{3} \frac{T_0}{T_s} \right]. \quad (51)$$

The total exergy received by the receiver from the heliostat field is

$$\dot{E}_{x,i} = \dot{Q}_r \left( 1 - \frac{T_0}{T_{hs}} \right). \quad (52)$$

Therefore, the exergy destroyed by the heliostat field is [49]

$$\dot{E}_{d,he} = \dot{E}_{x,s} - \dot{E}_{x,i}. \quad (53)$$

For the solar receiver, the exergy destruction is

$$\dot{E}_{d,rc} = \dot{Q}_{hs1} \left( 1 - \frac{T_0}{T_{hs}} \right) + \dot{m}((h_3 - h_4) - T_0(s_3 - s_4)), \quad (54)$$

The total exergy destroyed by the solar thermal plant,  $\dot{E}_{d,T}$ , the overall exergy yield  $\eta_{ex}$ , and the exergy yield of the thermal machine  $\eta_{exh}$  are defined as

$$\dot{E}_{d,T} = \dot{E}_{d,c} + \dot{E}_{d,t} + \dot{E}_{d,r} + \dot{E}_{d,a} + \dot{E}_{d,cc} + \dot{E}_{d,he} + \dot{E}_{d,rc}, \quad (55)$$

$$\eta_{ex} = P / (\dot{E}_{x,s} + \dot{m}_f E_{m,f}), \quad (56)$$

$$\eta_{exh} = P / \dot{m}((h_5 - h_3) - T_0(s_5 - s_3)) \quad (57)$$

Finally, estimate the fraction of destruction of each component as follows:

$$FE_{d,j} = \dot{E}_{d,j} / \dot{E}_{d,T} \quad (58)$$

#### 2.4. Description of the Working Fluids

The search for ways to increase the efficiency of different power cycles for gas turbines continues. In this sense, alternative working fluids are presented as a viable option in Brayton cycles, especially carbon dioxide, nitrogen, and some noble gases such as helium. Although the research is in its initial stages, some experimental activities have already been carried out in research centres without developing prototypes [6].

Supercritical carbon dioxide cycles are presented as very competitive options due to the high density and low compressibility of  $\text{CO}_2$  near the critical point that conduces to more compact equipment and higher efficiency process, i.e., the lesser work required in the compressor than other working fluids [25]. However, considering that the pressure ratio of the reference cycle is 9.9, this generates a maximum pressure of approximately 73 MPa, which makes it unfeasible from a technical point of view according to the maximum pressure in pipelines [55]. Therefore, the cycle is defined as a theoretical supercritical carbon dioxide cycle with  $r_p = 9.9$  ( $T\text{SCO}_2$ ) and its analysis is performed to compare the benefits of this type of configuration under the same conditions for the other cycles.

Additionally, the supercritical carbon dioxide cycle operating with  $r_p = 3.3$  is defined to achieve a technically applicable maximum pressure and is defined as ( $\text{SCO}_2$ ). The compressor inlet pressure for the supercritical cycles is  $p_1 = 7.4$  MPa. Additionally, subcritical carbon dioxide cycles are little studied [32] and do not present advantages over the supercritical ones regarding the significant reduction of the work required by the compressor. In this work, a subcritical carbon dioxide cycle is also applied in the same conditions as the air cycle, defined as ( $\text{CO}_2$ ). Another limitation that may exist in carbon dioxide cycles is the maximum temperature. In this sense, studies of possible reactions of the fluid with the materials have been carried out to reduce this possibility at maximum temperatures around 900 K [56]; however, some studies of these cycles reach temperatures above 1100 K [57].

According to other studies, the helium cycles present essential restrictions in the turbine's compressor system related to pressure changes in the size and design of blades and shafts [58]. The present study evaluates a transcritical helium cycle in which the reference pressure ratio of the Solugas project does not allow the operation of a regenerator with  $r_p = 9.9$  since the inequality  $T_6 > T_2$  is not fulfilled, as shown in Figure 3a. The  $p - T$  diagram shows that the turbine outlet temperature is lower than the compressor inlet temperature in the helium cycle. Results for simulation with helium without regenerator ( $\epsilon_r = 0$ ) are defined as  $He$ , while in the cases when the pressure ratio includes a helium cycle with regenerator ( $\epsilon_r = 0.775$ ), it is called  $He_r$  which only operates for low-pressure ratios. his work aims to perform a purely thermodynamic comparative analysis of the plant for different working fluids to evaluate its operation throughout an average day of the year and search for the best operating conditions in Barranquilla, Colombia. Given the above, aspects of turbomachine design, such as the number of passes and blade and shaft sizes, are not evaluated in detail, as Olumayegun et al. [59] described. The same irreversibilities are assumed for all cycles and pressure and mass flow ratios. The only property changes are to the compressor inlet pressure for the  $T\text{SCO}_2$  and  $\text{SCO}_2$  cycles, and the regenerator effectiveness ( $\epsilon_r = 0$ ) for the  $He$  cycle. The model is implemented in Modelica language using a Dymola compiler and free libraries for each fluid [59–61].

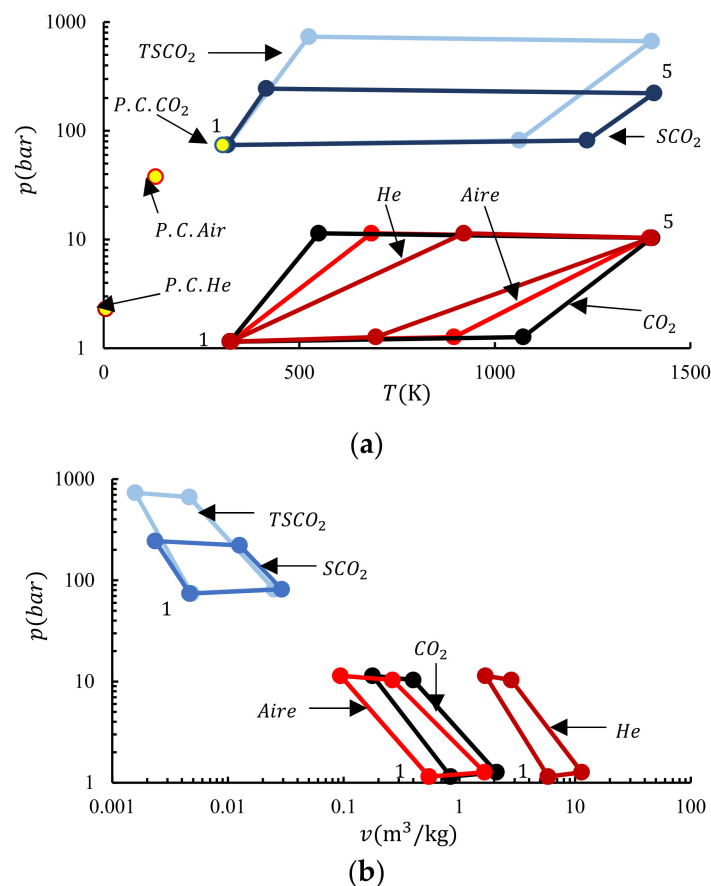


**Figure 3.**  $p - T$  diagram (a),  $p - v$  diagram (b), for the cycles with the different conditions to be simulated.

Figure 3a presents the pressure-temperature diagram using a logarithmic scale for the pressure in order to visualize the significant pressure changes in supercritical cycles between the maximum and minimum pressures. Additionally, it is observed that the inlet temperature of the compressor  $T_1$  and the turbine  $T_5$ , are similar in each cycle. However, the outlet temperatures of the compressor  $T_2$  and the turbine  $T_6$  change according to the working fluid. However, the outlet temperature of the turbine  $T_6$  is lower than the outlet temperature of the compressor  $T_2$  in the helium cycle. Additionally, the differences in the pressures of the supercritical cycles ( $TSCO_2$ ,  $SCO_2$ ) for the subcritical cycles ( $TSCO_2$ ,  $He$ ,  $Aire$ ) can be seen. With such pressures and temperatures, supercritical cycles are guaranteed to operate above the critical point of carbon dioxide [31]. Likewise, subcritical cycles are in the superheated steam region [32]. Additionally, Figure 3b shows the specific pressure-volume diagram. The temperature and specific volume scales are logarithmic to observe all the cycles in the same figure. However, according to the estimated values, the most significant pressure changes occur in the supercritical cycles, with values of 558.6 bar for the  $TSCO_2$  cycle, while for the subcritical cycles, the pressure change is 10.235 bar. Regarding the specific volume variations, the minimum changes occur in the supercritical cycles since the heat supply between states 2 and 5, the volume varies in  $0.044 \text{ m}^3/\text{kg}$ , and for the helium cycle, that value is  $1.13 \text{ m}^3/\text{kg}$ . Generally, the most considerable volume changes occur during this cycle, affecting power production.

### 3. Results and Discussion

This section presents the simulation results. The first part presents the comparative analysis of energy parameters such as power, overall plant efficiency, fuel consumption, and conversion rate. The second part presents the results of the exergy destruction of the cycles with their fluids and exergy efficiency.

### 3.1. Energy Analysis for Solar Radiation Conditions in Colombia

This section presents the results obtained for the energy analysis of the plant in Barranquilla after applying the DI radiation model and the thermodynamic model for the hybrid solar thermal plant validated, as shown in previous works [45,62]. The plant's ambient temperature and solar radiation conditions in Barranquilla are presented initially. Subsequently, the influence of the pressure ratio on the power produced, overall efficiency, and fuel conversion rate will be evaluated to find the optimum performance point.

For the simulation of the plant under that location conditions, the annual average values of  $\bar{H}_h = 6.24 \text{ kWh/m}^2/\text{day}$  and  $\bar{D}_h = 1.68 \text{ kWh/m}^2/\text{day}$  [43], and an annual average day  $n = 180$  are assumed. Figure 4 presents the  $I_{bh}$  for the annual mean values of radiation in Barranquilla (black squares). Additionally, the  $I_{bh}$  values for an average day of March when  $\bar{H}_h$  is maximum (blue squares) are presented for Barranquilla, compared to the  $I_{bh}$  values estimated for Seville (red circles) when  $\bar{H}_h$  is maximum in July. The hourly average temperature values for the city of Barranquilla taken from [63] are also presented to agree with the solar resource estimation, which will also be done every hour. Finally, a lower heating value of  $42624 \text{ kJ/kg}$  is taken from Gas Natural S.A. ESP's natural gas quality report.

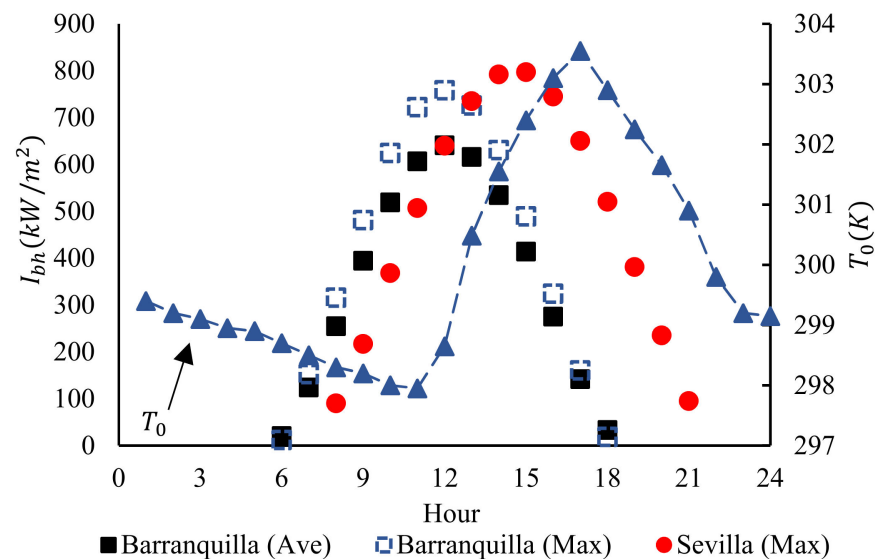
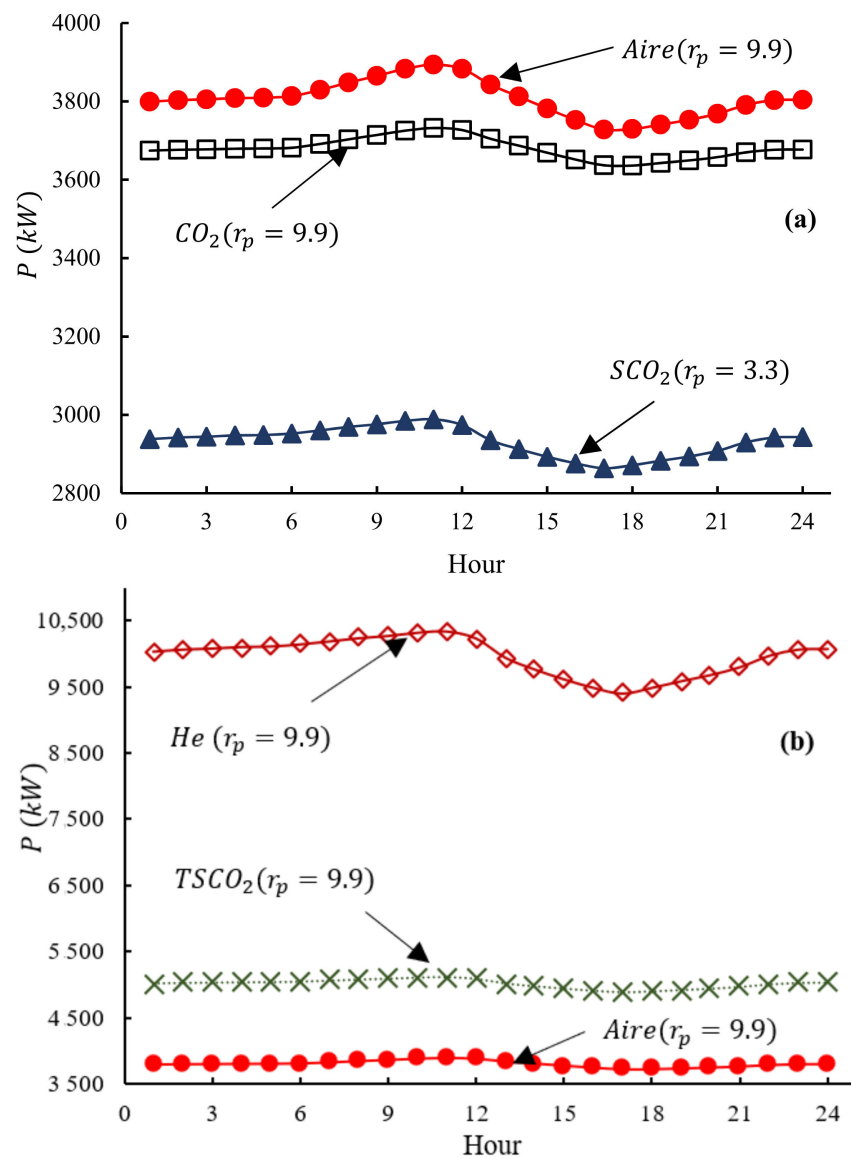


**Figure 4.** Comparison of  $I_{bh}$  for Seville and Barranquilla.

### 3.2. Plant Energy Analysis

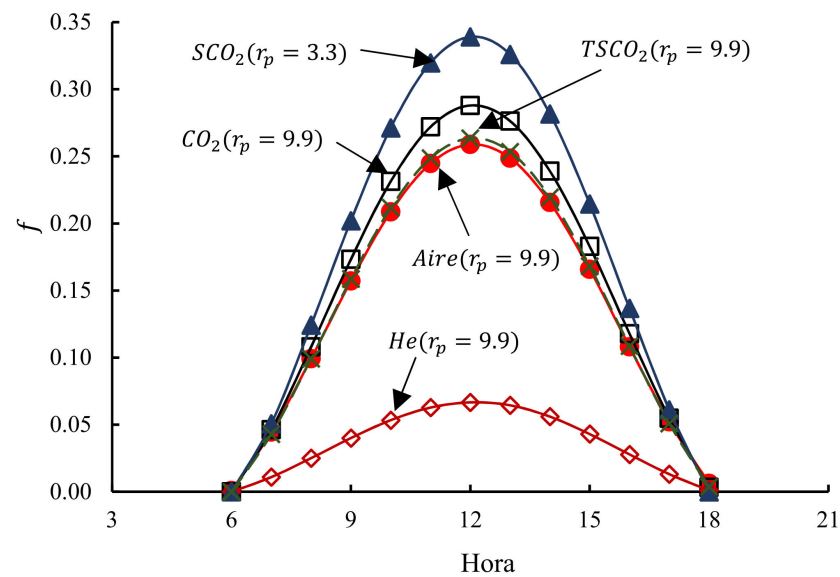
This section presents the plant simulation results for the energy variables for different configurations with their working fluids. Initially, the power produced, overall efficiency, fuel consumption, and fuel conversion rate throughout the day are evaluated; finally, the influence of the pressure ratio on the power and overall efficiency is also analysed.

Figure 5 shows the CSP net power for the mentioned configuration in Section 2.2, including results for the air cycle, which will be used as a reference. Figure 5a shows that the  $\text{CO}_2$  cycle generates an average power of  $3680.03 \text{ kW}$ , 3.3% lower than the average power of the air cycle. On the other hand, the  $\text{SCO}_2$  cycle generates the lowest power with an average value of  $2952.34 \text{ kW}$ , 22.9% lesser than the power obtained for the cycle operating with air as a working fluid. However, it should be considered that it has the lowest pressure ratio value ( $r_p = 3.3$ ) compared with the operation with other fluids.



**Figure 5.** Power evolution throughout the day. (a) shows that the  $CO_2$  cycle generates an average power of 3680.03 kW, 3.3% lower than the average power of the air cycle; (b) shows results for the  $TSCO_2$  cycle with an average power generation of 5018 kW, and the helium ( $He$ ) cycle with an average power of 9957.39 kW.

On the other hand, Figure 5b shows results for the  $TSCO_2$  cycle with an average power generation of 5018 kW, and the helium ( $He$ ) cycle with an average power of 9957.39 kW. These cycles deliver more power, 31.8% and 161% higher, respectively than the 3806.11 kW produced by the air cycle. This increase in the power of the  $TSCO_2$  cycle is understood as a purely theoretical cycle given the maximum pressures it handles. Instead, the power increases significantly in the Helium cycle due to its high specific heat, as described above. However, as shown in the following analysis, this is at the expense of lower efficiency and higher fuel consumption. Figure 6 presents the variation of the solar fraction ( $f$ ) as a function of the presented fluid configurations. It is observed that  $f$ , for the cycle with  $TSCO_2$  at noon, is only 1.9% lower than the air cycle. On the other hand, the  $CO_2$  and  $SCO_2$  cycles show an increase in  $f$  of 11.2% and 30.9% for the air cycle at noon. Finally, the helium ( $He$ ) cycle shows a 74.2% decrease concerning air when  $f = f_{max}$ .



**Figure 6.** Evolution of the solar fraction in the daytime.

Considering that solar radiation is maximum around noon (see Figure 4), the solar fraction  $f$  (see Figure 6) will also be maximum at that time; this will be considered for subsequent analyses. Figure 7 shows the working fluid influence on the cycle's overall efficiency. Regarding the  $SCO_2$  cycle, it has an overall efficiency 6.7% higher than that of the average air when  $f = 0$  (at night hours), but it is 2.2% lower when  $f = f_{max}$  at noon. Additionally, the  $CO_2$  cycle has the average overall efficiency 9.1% higher than that of air when no solar input occurs ( $f = 0$ ) and 6.1% higher for  $f = f_{max}$ .

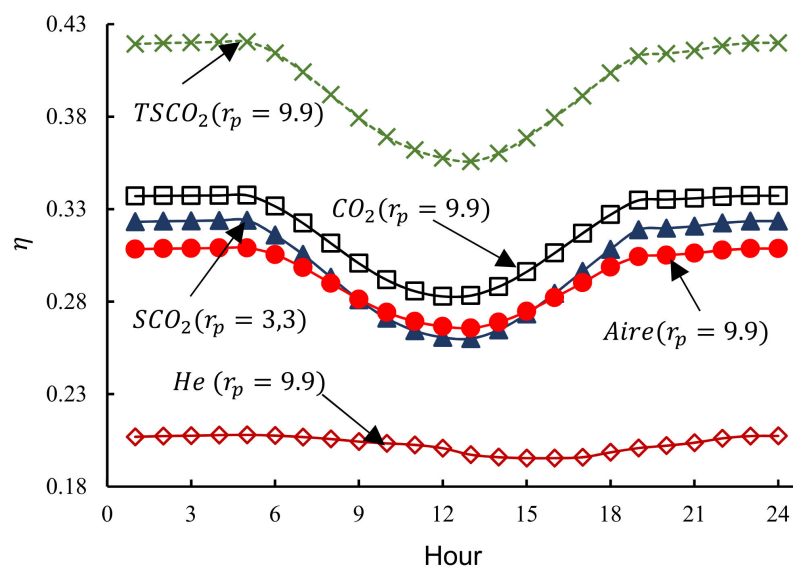


**Figure 7.** Evolution of overall efficiency in the day.

Additionally, Figure 7 shows the efficiency curve for the cycle using  $TSCO_2$ . This is the condition with the highest overall efficiency, with an average increase of 35.8% when  $f = 0$  and 34.1% when  $f = f_{max}$  concerning the cycle operating with air. It is essential to highlight that the helium cycle does not operate with a regenerator for that pressure ratio, as explained before. This implies that more heat must be supplied from the combustion chamber and, therefore, the overall efficiency is reduced. Likewise, the influence of the solar concentration system on  $\eta$ , when the solar resource is available, is lower because the solar fraction  $f$  decreases drastically, as shown below.

Figure 8 presents the fuel consumption for the cycle operating with different working fluids. As observed in the case of the solar fraction, the fuel consumption for the cycle with  $TSCO_2$  is very close to the air cycle with a difference of less than 3%. In contrast, the cycle with  $CO_2$  shows a decrease in fuel consumption between 11.5% and 15%; however, the cycle operating with  $SCO_2$  has a decreased consumption between 26% and 34.2%, concerning the air cycle when  $f = 0$  and  $f = f_{max}$ , respectively. Finally, the helium cycle shows an increase in fuel consumption between 291% and 394%, when  $f = 0$  and when  $f = f_{max}$ , respectively. The significant increase in the helium cycle fuel consumption is related to its higher specific heat compared to other working fluids.

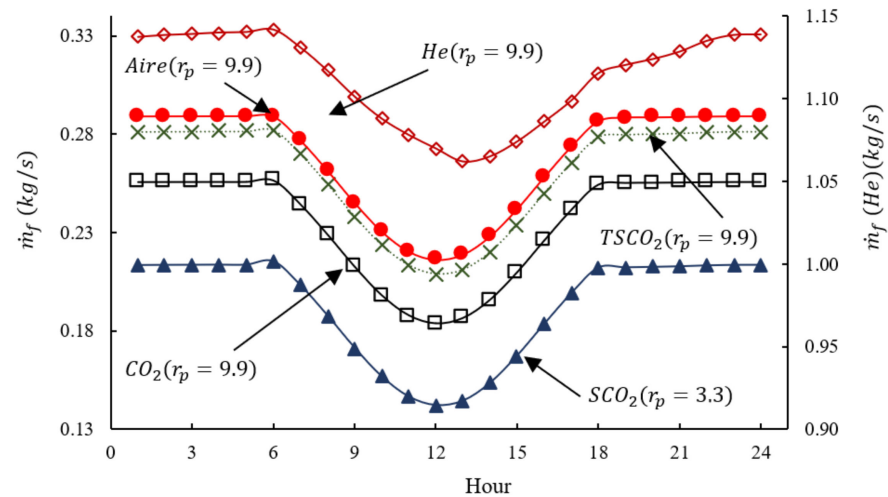


Figure 8. Evolution of fuel consumption during the day.

On the other hand, Figure 9 presents the plant's fuel conversion factor evolution. It is observed that, in general, the carbon dioxide cycles have better performance, with the cycle with  $TSCO_2$  being the best with an increase in  $r_e$  of 35.9% to the air cycle when  $f = f_{max}$ . Additionally, in the cycles with  $SCO_2$  and  $CO_2$ , the value of  $r_e$  is 16.4% and 13% higher than the air cycle when the solar fraction is a maximum. Finally, the helium cycle presents the lowest value of fuel conversion factor, which is 46.7% lower than the air cycle when  $f$  is maximum.

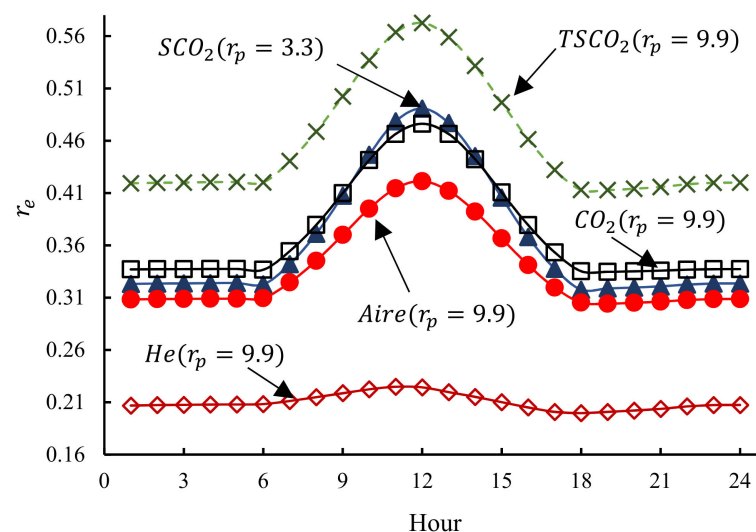
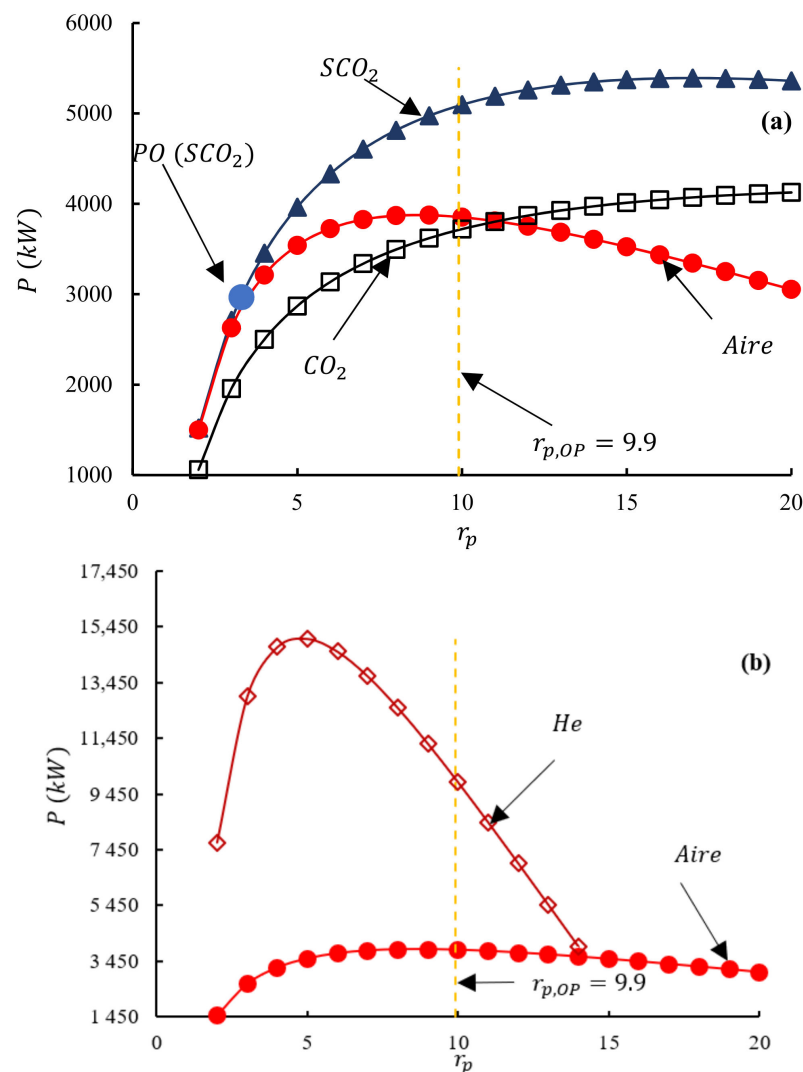


Figure 9. Evolution of the fuel conversion factor over the day.

Figure 10a shows the power cycle curves as a function of pressure ratio variation for the supercritical cycles ( $TSCO_2$ ,  $SCO_2$ ), the air cycle, and the  $CO_2$  cycle. It is observed that

the supercritical cycles present the highest power values; however, it starts to decrease after  $r_p = 17$  where the maximum power is presented and, at the operating point ( $r_p = 9.9$ ), presenting values 31.9% higher than the air cycle. The  $\text{CO}_2$  cycle has lower power values than the air cycle for low-pressure ratios; however, the power grows continuously within the range studied. Additionally, the air cycle power is only 3.7% higher compared to the  $\text{CO}_2$  cycle at the operating point. Eventually, the power continuously grows in the range of pressures from 2 to 20, surpassing the power delivered by the air cycle. Figure 10b presents the evolution of the power values of the helium cycle, where it is observed that, that with this working fluid, it is possible to produce more power than the studied cycles; however, the maximum power is obtained at  $r_p = 4.8$ . Then, it decreases significantly to zero at  $r_p = 17$  due to the compressor's excessive power consumption. Finally, the air cycle maximum power occurs at  $r_p = 8.9$ .



**Figure 10.** Influence of pressure ratio on cycle power. (a) shows the power cycle curves as a function of pressure ratio variation for the supercritical cycles ( $\text{TSCO}_2$ ,  $\text{SCO}_2$ ), the air cycle, and the  $\text{CO}_2$  cycle; (b) presents the evolution of the power values of the helium cycle, where it is observed that, that with this working fluid, it is possible to produce more power than the studied cycles; however, the maximum power is obtained at  $r_p = 4.8$ .

Figure 11 shows the variation of  $\eta$  concerning  $r_p$  when  $f$  is maximum. It can be seen that the cycle with the highest overall efficiency occurs when carbon dioxide in supercritical conditions is used, finding its maximum value at  $r_p = 11.3$ . On the other

hand, the air cycle which finds its maximum at  $r_p = 6.3$ , presents an intermediate efficiency at low-pressure ratios and is surpassed by the  $CO_2$  cycle after  $r_p = 8$ , the latter reaching its maximum at  $r_p = 15.4$ . The helium cycle without regeneration has the lowest overall efficiency and presents its maximum overall efficiency at  $r_p = 6.8$ . However, when including the regenerator, the regenerative helium cycle  $He_r$ , the increase in efficiency is significant, being close to the maximum of the air and  $CO_2$  cycles. Nevertheless, its maximum efficiency is given at values of  $r_p = 3.4$  and, from  $r_p = 6$ , the regenerative cycle does not apply because the inequality  $T_6 > T_2$  is not fulfilled.

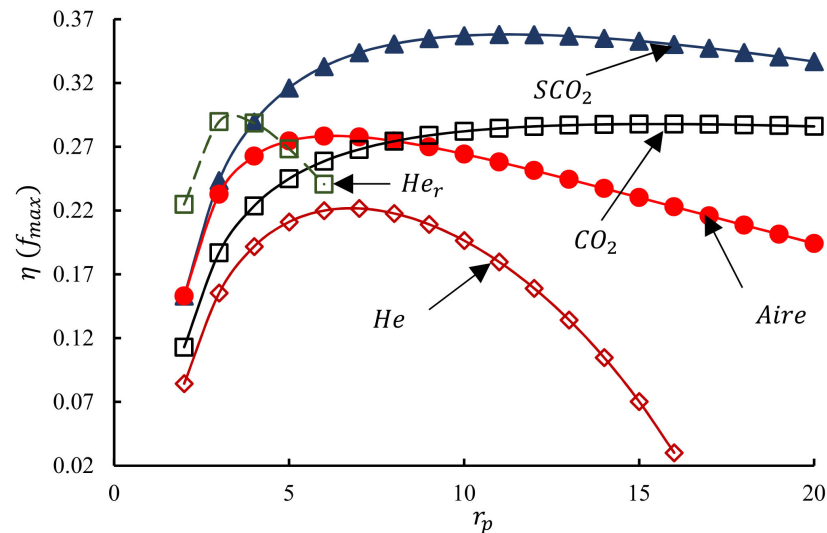


**Figure 11.** Influence of pressure ratio on overall cycle efficiency.

Finally, Figure 12 presents values for fuel conversion factor when  $f = f_{max}$  as a function of pressure ratio. It can be observed that the highest values of  $r_e$  are achieved when the cycle uses carbon dioxide in supercritical conditions reaching the maximum at  $r_p = 8.2$ . On the other hand, the helium cycles present lower economic efficiency values, especially the He cycle. Meanwhile, the  $He_r$  cycle is the second cycle with the lowest  $r_e$  value when the solar input is maximum. The  $CO_2$  cycle outperforms in economic efficiency the air cycle from  $r_p$  higher than 7, both having intermediate economic efficiencies for the other working fluids.

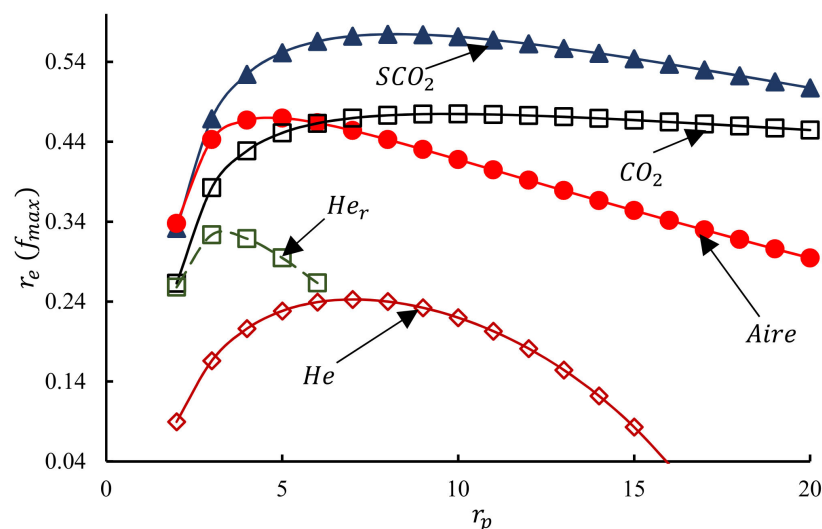


**Figure 12.** Influence of pressure ratio on fuel conversion rate.

### 3.3. Exergy Analysis of the Hybrid Solar Thermal Plant

This section presents the exergy analysis of the solar thermal plant. First, as presented in Section 2.3, the exergy destruction is estimated from each state's enthalpy and entropy values within the power cycle and the operating conditions of the solar concentrating system. In addition, the exergy destruction for the combustion chamber, its heat exchanger, and the fuel and combustion products must be estimated with the amount of air required for combustion. According to the above, to estimate the fuel exergy, the molar composition of the natural gas is taken from the quality report of Gas Natural S.A. ESP, and the standard chemical exergy [64] and the molar mass of each component in the fuel are obtained [31]. Then, this information is replaced in Equation (50) to estimate the fuel-specific exergy in kJ/kmol, obtaining:

$$E_{q,f} = 898,177.092 + 8.314T_0(-0.449189975). \quad (59)$$

Therefore, the natural gas chemical exergy,  $E_{q,f}$ , is divided by the natural gas molar mass obtained in a weighted average for its components [46], giving a value of  $PM_{m,f} = 18.1749059$  kg/kmol. This guarantees that the units for the specific exergy of natural gas,  $E_{m,f}$ , are in kJ/kg. To estimate the chemical exergy of the combustion air, the same process was carried out, taking as reference normal air with 21%  $H_2$  and 79%  $N_2$ . Regarding the exhaust gases, combustion analysis was performed with 300% excess air to ensure complete combustion. Then, the amount of air that enters the combustion chamber was estimated, being  $\dot{m}_a = 48.82 \dot{m}_f$ .

The exergy destruction analysis is performed at the same instants where the solar model estimates the  $I_{bh}$ , including ambient temperature  $T_0$  variations. Figure 13 shows the evolution of the total exergy destruction for each cycle. It can be observed that the cycles destroy little or nothing exergy when no solar resource is present, with a remarkable influence of the ambient temperature on its variation. However, as solar radiation increases and the concentrating system starts operation, the exergy destruction of these components begins to rise. Therefore, the total exergy destruction increases until it reaches a maximum around noon when the solar fraction is at its extreme. Figure 13 also shows that the cycle that destroys more exergy operates with helium. This cycle presents total exergy destruction on average 352% higher than the air cycle when no solar resource is present due to its higher fuel consumption (see Figure 8). Additionally, the carbon dioxide cycles show lower exergy destruction than the air cycle in a similar way to fuel consumption, with lesser total exergy destruction in the  $SCO_2$  cycle.

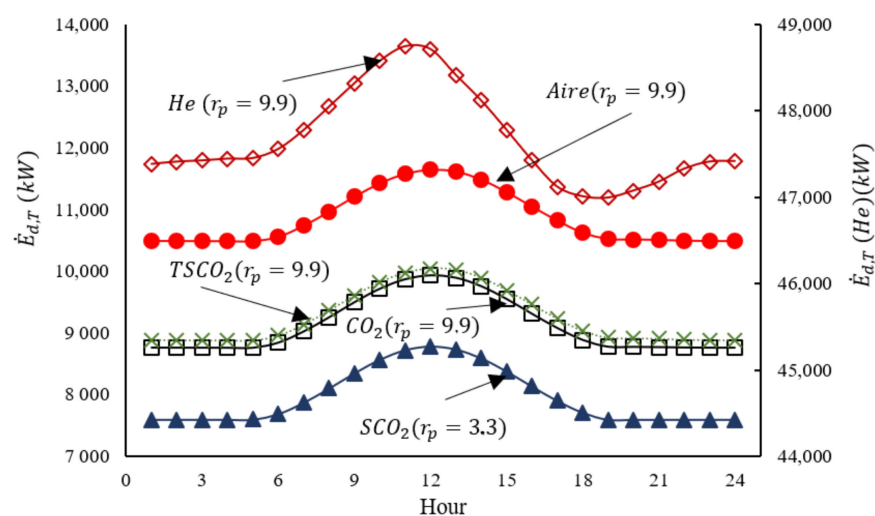


Figure 13. Evolution of total exergy destruction for each cycle.

Figure 14 shows the fraction of exergy destruction to the total exergy destroyed variation in each cycle component operating with air; fractions variation at night is minimal. This change when the solar resource becomes available, increasing the exergy destruction in its components and reducing it in the combustion chamber. Additionally, Table 1 shows the comparative values of the exergy destruction fraction for the component when  $f = 0$  (average values) and  $f = f_{max}$ . It can be observed that when the solar fraction is maximum, the exergy destruction fraction in the heliostat field reaches a maximum of 0.1891, while this fraction is 0.05418 in the receiver. On the other hand, the exergy destruction fraction decreases in the other components, especially in the combustion chamber, where it is reduced by 34.6 % and 10% in the other components.

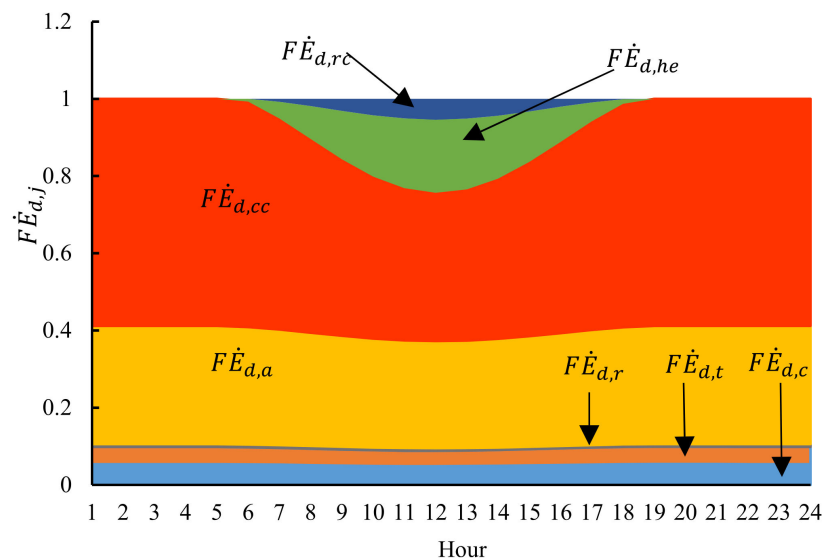
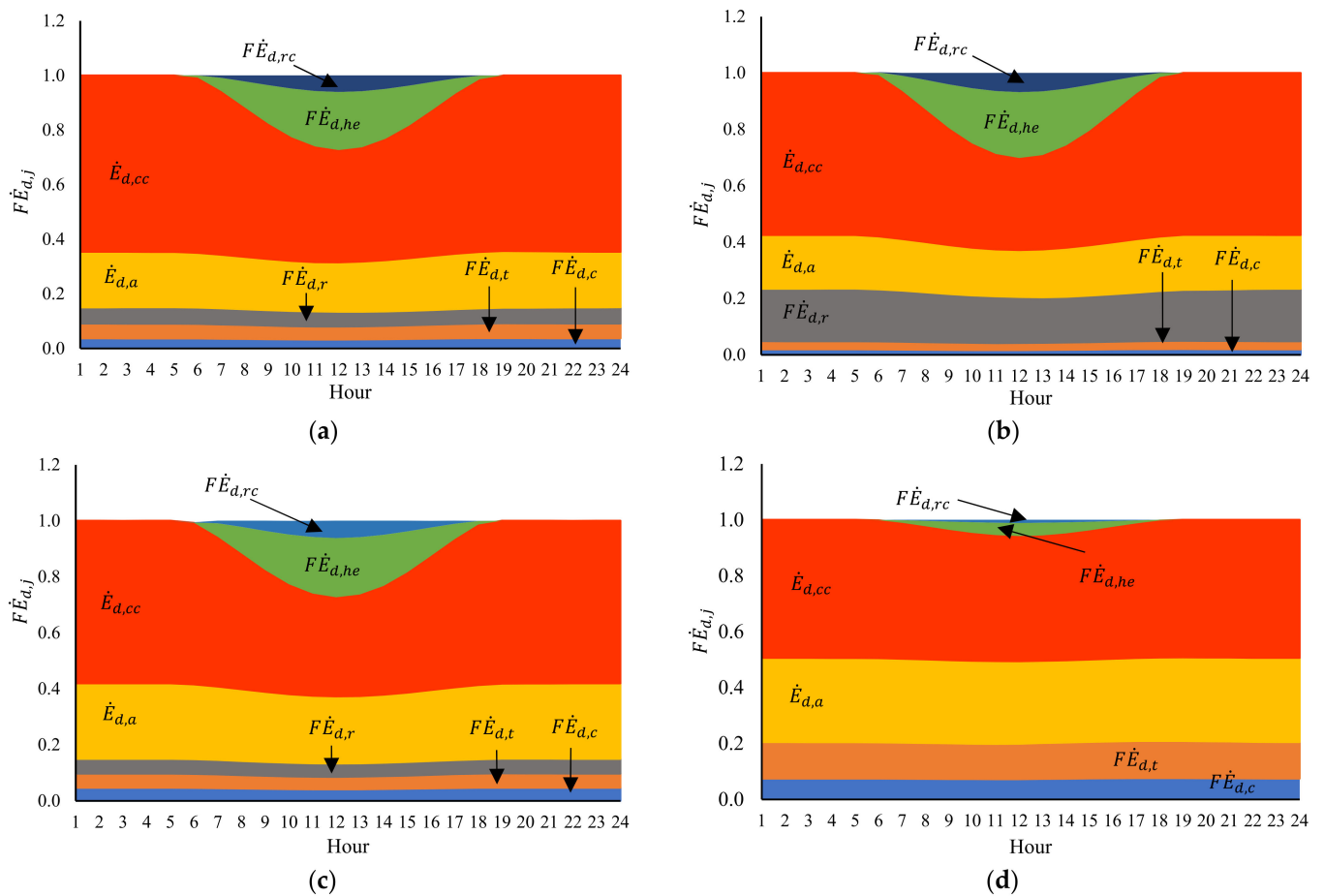


Figure 14. Evolution of the exergy destruction fraction of each component within the air cycle.

Table 1. Fraction of exergy destroyed in each component of the cycle with air.

Exergy Destruction Fractions	Night (Average)	12 m (Noon)
$F\dot{E}_{d,t}$ (Turbine)	0.05421	0.048560
$F\dot{E}_{d,c}$ (Compressor)	0.07169	0.064210
$F\dot{E}_{d,r}$ (Regenerator)	0.00709	0.006932
$F\dot{E}_{d,a}$ (Environmental H. E.)	0.2948	0.266884
$F\dot{E}_{d,cc}$ (Combustion Chamber)	0.57219	0.369223
$F\dot{E}_{d,he}$ (Heliostat Field)	0	0.189661
$F\dot{E}_{d,rc}$ (Central Receptor)	0	0.054451

Figure 15 presents the evaluation of the exergy destruction fraction of each component during the simulated day for the studied working fluids. Figure 15a presents the exergy destruction fraction for the  $TSCO_2$  cycle; it is observed that  $F\dot{E}_{d,cc}$  is 0.6444 when no solar resource is present, which is 11.8% higher than the air cycle. The exergy destruction fraction for the heat exchanger to the environment and regenerator is 27.8% and 716% higher in the  $TSCO_2$  for the air cycle. In the supercritical carbon dioxide cycle ( $r_p = 9.9$ ) the solar concentrating system fraction  $F\dot{E}_{d,he}$  and  $F\dot{E}_{d,rc}$ , are 11.8% and 11.2% higher than the air cycle. Given the above, it is observed that although the  $TSCO_2$  cycle destroys less exergy than the air cycle (see Figure 13), some fractions, such as those observed for the combustor, heat exchanger to the environment, and solar concentrating systems, are higher than in the air cycle, while the turbine and compressor fractions remain at lower values.



**Figure 15.** Evolution of the exergy destruction fraction of each component for the cycles  $TSCO_2$  (a),  $SCO_2$  (b),  $CO_2$  (c), and  $He$  (d).

Figure 15b presents the exergy destruction fraction of the  $SCO_2$  cycle ( $r_p = 3.3$ ), where the highest value is observed in the combustor chamber, which is only 0.3% higher than that of the air cycle; however, the  $F\dot{E}_{d,a}$  value is 34.6% lower than that of the air cycle. The solar concentration system fractions  $F\dot{E}_{d,he}$  and  $F\dot{E}_{d,rc}$  are 23% and 25% higher in the supercritical carbon dioxide cycle ( $r_p = 9.9$ ) compared to the air cycle. In the carbon dioxide cycles, the exergy destruction fraction in the compressor and turbine is lower than that of the air cycle; in this case,  $F\dot{E}_{d,c}$  and  $F\dot{E}_{d,t}$  are lower by 63.8% and 59.5%, respectively, concerning the air cycle. In addition, the exergy destruction in the regenerator is higher due to the pressure ratio reduction and, therefore, to the higher heat exchange in this equipment.

Figure 15c shows the exergy destruction in the subcritical carbon dioxide cycle. Since the fuel and power consumption are similar to those for the air cycle, the exergy destruction values are also similar in both cycles; however, the  $F\dot{E}_{d,r}$  value is 638% higher than that of the air cycle, mainly because of the significant difference between the compressor's and the turbine's outlet temperature and the higher heat transfer in the regenerator. Finally, Figure 15d shows the exergy destruction in the cycle operating with helium, where it is observed that the  $F\dot{E}_{d,r}$  value is zero, and the values of  $F\dot{E}_{d,c}$  and  $F\dot{E}_{d,t}$  are, respectively, 67.5% and 142% higher than the values of the air cycle. The exergy destruction fractions of the combustor and the heat exchanger to the environment are lower than the values of the air cycle. The  $F\dot{E}_{d,he}$  and  $F\dot{E}_{d,rc}$  fractions barely reach values of 0.05706 and 0.01109 when the solar input is maximum.

Figure 16 shows the CSP global exergy efficiency variation ( $\eta_{ex}$ ) for the cycles operating with  $TSCO_2$ ,  $CO_2$  and  $SCO_2$ . where increases of 35.9%, 9.8%, and 5%, respectively, at  $f = 0$  with respect to the air cycle are observed. Meanwhile, when  $f = f_{max}$  the upsurges are

34.4%, 6.9%, and 0.1% concerning the air cycle. Additionally, the cycle with helium presents a decrease of 33% when  $f = 0$  and 33.2% when  $f = f_{max}$ .

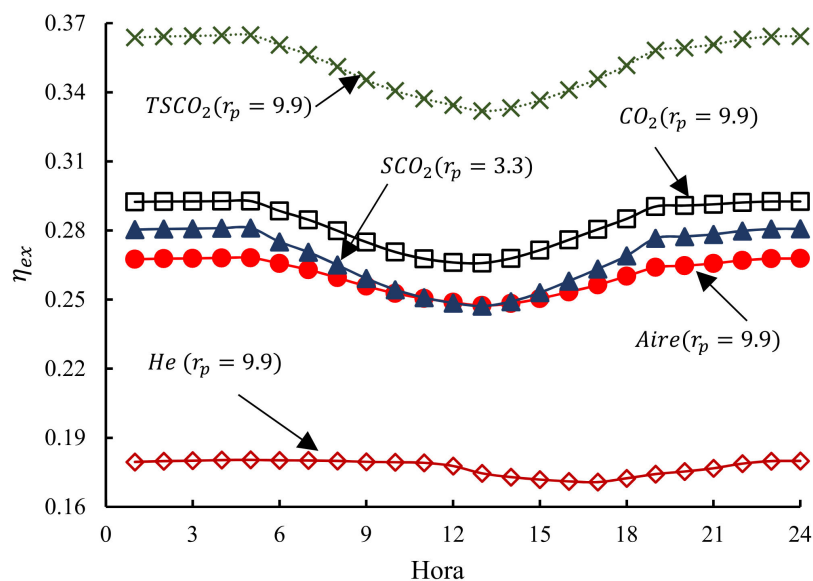


Figure 16. Evolution of global exergy efficiency during the day.

Finally, Figure 17 presents the pressure ratio influence on  $\eta_{ex}$  values for the case with a higher solar factor. It is observed that the curves are very similar to the energy efficiency. In this case, the higher energy efficiency values correspond to the supercritical carbon dioxide cycle that reaches its maximum point at values of  $r_p = 10.9$  with a value of 0.3354. Conversely, the cycle operating with helium presents the lowest values of  $\eta_{ex}$  whose maximum value is 0.1956 at values of  $r_p = 6.8$ . The air and  $CO_2$  cycles have intermediate exergy efficiency values. Additionally, it is observed that the helium cycle with a regenerator can increase the exergy efficiency but at low  $r_p$  values.

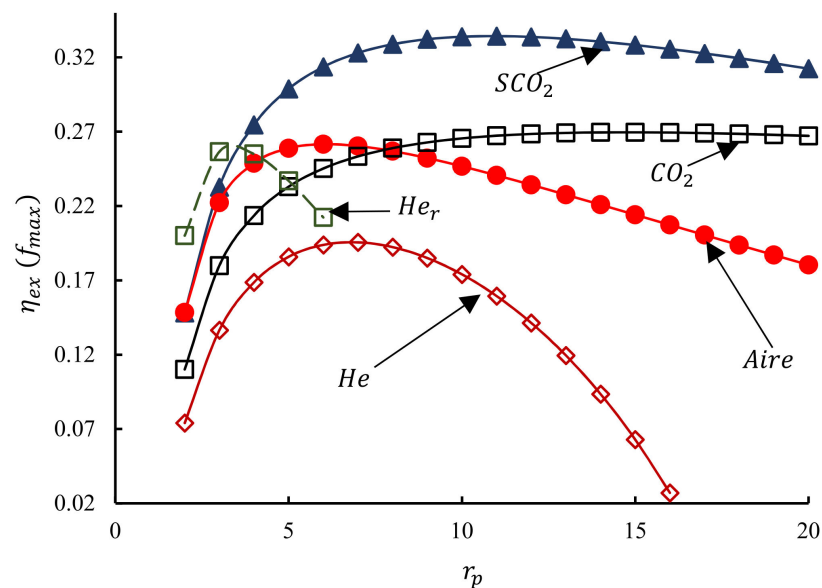


Figure 17. Influence of pressure ratio on global exergy efficiency.

#### 4. Conclusions

In this work, the carbon dioxide cycle was evaluated under supercritical conditions. This is an excellent option as a variant to air cycles since its overall efficiency is higher by

40% at its operating point (PO) and 38% at its maximum efficiency point (PM). Although the maximum pressure limits its operation, it can generate more power, which makes it necessary to limit its pressure ratio. Additionally, it was observed that, at a limited pressure ratio of 3.3, efficiencies are close to the air cycle with  $r_p$  of 9.9. This implies lower fuel consumption at low-pressure ratios and higher efficiencies at higher pressure ratios. Additionally, this cycle's exergy destruction is also inferior; therefore, the exergy efficiency is higher than that of air, 27.2% at the points of maximum exergy efficiency. Finally, the subcritical carbon dioxide cycle, operating under the same conditions as the air cycle, allows us to obtain a similar power output with slightly lower fuel consumption, with it being possible to have an overall and exergy efficiency higher than the air cycle in 9.4% and 9.3%, respectively, for  $r_p = 9.9$ .

The helium cycle was initially simulated without considering the presence of a regenerator because, at  $r_p = 9.9$  the turbine outlet temperature is lower than the compressor outlet temperature. From the operation of the hybrid cycle with this working fluid, 161% more power can be generated than the air cycle due to its high specific heat and adiabatic coefficient. However, the fuel consumption is 394% higher than the air cycle, so efficiencies are inferior. Similarly, the energy efficiency is lower than in the other cases due to the high fuel consumption, resulting in a lower solar fraction.

Finally, the cycles operating with carbon dioxide show the best performance, presenting their maximum power values at pressure ratios higher than 16, while the air cycle presents maximum power values at pressure ratios lower than 9. Concerning energy and energy efficiencies, the carbon dioxide cycles reach their maximum values at pressure ratios higher than 10, while the cycles with other working fluids have pressure ratios lower than this value. In this sense, the cycles with helium without a regenerator present the maximum energy and exergy efficiency values in pressure ratio values close to 7. In contrast, the helium regenerative cycle presents its maximum with pressure ratio values between 3 and 4. Therefore, after analysing the results, the carbon dioxide cycles are presented as an attractive option given their higher efficiency, especially the supercritical cycles at low-pressure ratios and the subcritical ones at high-pressure ratios.

**Author Contributions:** Conceptualization, F.M.-G. and C.N.-L.; methodology, F.M.-G. and C.N.-L.; validation, F.M.-G. and C.N.-L.; formal analysis, F.M.-G. and C.N.-L.; investigation, F.M.-G. and C.N.-L.; writing—original draft preparation, F.M.-G., A.E.-A. and C.N.-L.; writing—review and editing, F.M.-G., A.E.-A. and C.N.-L.; supervision, A.E.-A. and C.N.-L. All authors have read and agreed to the published version of the manuscript.

**Funding:** This research was partially funded by Universidad Francisco de Paula Santander.

**Acknowledgments:** The authors would like to thank Universidad Francisco de Paula Santander for providing the computer equipment, the Dymola license, and the doctoral studies commission of the author Faustino Moreno.

**Conflicts of Interest:** The authors declare no conflict of interest.

## References

1. Chen, L.; Zhang, W.; Sun, F. Power, efficiency, entropy-generation rate and ecological optimization for a class of generalized irreversible universal heat-engine cycles. *Appl. Energy* **2007**, *84*, 512–525. [[CrossRef](#)]
2. Obaideen, K.; AlMallahi, M.N.; Al-Alami, A.H.; Ramadan, M.; Abdelkareem, M.A.; Shehata, N.; Olabi, A. On the contribution of solar energy to sustainable developments goals: Case study on Mohammed bin Rashid Al Maktoum Solar Park. *Int. J. Thermofluids* **2021**, *12*, 100123. [[CrossRef](#)]
3. Mills, D. Advances in solar thermal electricity technology. *Sol. Energy* **2004**, *76*, 19–31. [[CrossRef](#)]
4. Najjar, Y.S.; Zaamout, M.S. Comparative performance of closed cycle gas turbine engine with heat recovery using different gases. *Heat Recover. Syst. CHP* **1992**, *12*, 489–495. [[CrossRef](#)]
5. Al-Attab, K.; Zainal, Z. Externally fired gas turbine technology: A review. *Appl. Energy* **2015**, *138*, 474–487. [[CrossRef](#)]
6. Olumayegun, O.; Wang, M.; Kelsall, G. Closed-cycle gas turbine for power generation: A state-of-the-art review. *Fuel* **2016**, *180*, 694–717. [[CrossRef](#)]
7. Ulrich, H. *Closed-Cycle Gas Turbines: Operating Experience and Future Potential*; ASME Press: New York, NY, USA, 2005.

8. Wright, D.E.; Tignac, L.L. Status Report—Advanced Heat Exchanger Technology for a CCGT Power Generation System. *J. Eng. Power* **1983**, *105*, 348–353. [[CrossRef](#)]
9. Holt, C.F.; Boiarski, A.A.; Carlton, H.E. The Gas Turbine Heat Exchanger in the Fluidized Bed Combustor. *J. Eng. Power* **1983**, *105*, 438–445. [[CrossRef](#)]
10. Abram, T.; Ion, S. Generation-IV nuclear power: A review of the state of the science. *Energy Policy* **2008**, *36*, 4323–4330. [[CrossRef](#)]
11. Vera, D.; Jurado, F.; Carpio, J. Study of a downdraft gasifier and externally fired gas turbine for olive industry wastes. *Fuel Process. Technol.* **2011**, *92*, 1970–1979. [[CrossRef](#)]
12. Pantaleo, A.; Camporeale, S.; Shah, N. Thermo-economic assessment of externally fired micro-gas turbine fired by natural gas and biomass: Applications in Italy. *Energy Convers. Manag.* **2013**, *75*, 202–213. [[CrossRef](#)]
13. Cocco, D.; Deiana, P.; Cau, G. Performance evaluation of small size externally fired gas turbine (EFGT) power plants integrated with direct biomass dryers. *Energy* **2006**, *31*, 1459–1471. [[CrossRef](#)]
14. Soltani, S.; Mahmoudi, S.; Yari, M.; Rosen, M. Thermodynamic analyses of an externally fired gas turbine combined cycle integrated with a biomass gasification plant. *Energy Convers. Manag.* **2013**, *70*, 107–115. [[CrossRef](#)]
15. Dunham, M.T.; Iverson, B.D. High-efficiency thermodynamic power cycles for concentrated solar power systems. *Renew. Sustain. Energy Rev.* **2014**, *30*, 758–770. [[CrossRef](#)]
16. Heller, P.; Pfänder, M.; Denk, T.; Tellez, F.; Valverde, A.; Fernandez, J.; Ring, A. Test and evaluation of a solar powered gas turbine system. *Sol. Energy* **2006**, *80*, 1225–1230. [[CrossRef](#)]
17. Chen, Y.; Cheng, Y.; Sun, M. Physical Mechanisms on Plasmon-Enhanced Organic Solar Cells. *J. Phys. Chem. C* **2021**, *125*, 21301–21309. [[CrossRef](#)]
18. Chen, Y.; Cheng, Y.; Sun, M. Nonlinear plexitons: Excitons coupled with plasmons in two-photon absorption. *Nanoscale* **2022**, *14*, 7269–7279. [[CrossRef](#)]
19. Barigozzi, G.; Perdichizzi, A.; Gritti, C.; Guaiatelli, I. Techno-economic analysis of gas turbine inlet air cooling for combined cycle power plant for different climatic conditions. *Appl. Therm. Eng.* **2015**, *82*, 57–67. [[CrossRef](#)]
20. Livshits, M.; Kribus, A. Solar hybrid steam injection gas turbine (STIG) cycle. *Sol. Energy* **2012**, *86*, 190–199. [[CrossRef](#)]
21. Olivenza-León, D.; Medina, A.; Calvo-Hernández, A. Thermodynamic modeling of a hybrid solar gas-turbine power plant. *Energy Convers. Manag.* **2015**, *93*, 435–447. [[CrossRef](#)]
22. Santos, M.; Merchán, R.; Medina, A.; Hernández, A.C. Seasonal thermodynamic prediction of the performance of a hybrid solar gas-turbine power plant. *Energy Convers. Manag.* **2016**, *115*, 89–102. [[CrossRef](#)]
23. Merchán, R.; Santos, M.; Reyes-Ramírez, I.; Medina, A.; Hernández, A.C. Modeling hybrid solar gas-turbine power plants: Thermodynamic projection of annual performance and emissions. *Energy Convers. Manag.* **2017**, *134*, 314–326. [[CrossRef](#)]
24. Liu, Y.; Wang, Y.; Huang, D. Supercritical CO<sub>2</sub> Brayton cycle: A state-of-the-art review. *Energy* **2019**, *189*, 115900. [[CrossRef](#)]
25. Kulhánek, M.; Dostál, V. Supercritical carbon dioxide cycles thermodynamic analysis and comparison. In *Supercritical CO<sub>2</sub> Power Cycle, Proceedings of Supercritical CO<sub>2</sub> Power Cycle Symposium, Troy, NY, USA, 29–30 April 2009*; EEUU: Boulder, CO, USA, 2011.
26. Liao, J.; Liu, X.; Zheng, Q.; Zhang, H. Analysis of the power generation cycle characteristics of supercritical carbon dioxide. *J. Eng. Therm. Energy Power* **2016**, *31*, 40–46.
27. Wang, X.; Yang, Y.; Zheng, Y.; Dai, Y. Exergy and exergoeconomic analyses of a supercritical CO<sub>2</sub> cycle for a cogeneration application. *Energy* **2017**, *119*, 971–982. [[CrossRef](#)]
28. Wang, X.; Dai, Y. Exergoeconomic analysis of utilizing the transcritical CO<sub>2</sub> cycle and the ORC for a recompression supercritical CO<sub>2</sub> cycle waste heat recovery: A comparative study. *Appl. Energy* **2016**, *170*, 193–207. [[CrossRef](#)]
29. Akbari, A.D.; Mahmoudi, S.M. Thermo-economic analysis & optimization of the combined supercritical CO<sub>2</sub> (carbon dioxide) recompression Brayton/organic Rankine cycle. *Energy* **2014**, *78*, 501–512. [[CrossRef](#)]
30. Bae, S.J.; Ahn, Y.; Lee, J.; Lee, J.I. Hybrid system of Supercritical Carbon Dioxide Brayton cycle and carbon dioxide Rankine cycle combined fuel cell. In *Proceedings of the ASME Turbo Expo, Düsseldorf, Germany, 16–20 June 2014*; Volume 3B.
31. Cengel, Y.A.; Boles, M.E. *Thermodynamics: An Engineering Approach*; McGraw-Hill: New York, NY, USA, 2012.
32. Santos, M.; Miguel-Barbero, C.; Merchán, R.; Medina, A.; Hernández, A.C. Roads to improve the performance of hybrid thermosolar gas turbine power plants: Working fluids and multi-stage configurations. *Energy Convers. Manag.* **2018**, *165*, 578–592. [[CrossRef](#)]
33. McDonald, C.F. Helium turbomachinery operating experience from gas turbine power plants and test facilities. *Appl. Therm. Eng.* **2012**, *44*, 108–142. [[CrossRef](#)]
34. Bamnert, K.; Groschup, G. Status report on closed-cycle power plants in the federal republic of Germany. *J. Eng. Gas Turbines Power* **1977**, *99*, 37–46. [[CrossRef](#)]
35. Baxi, C.; Telengator, A.; Razvi, J. Rotor scale model tests for power conversion unit of GT-MHR. *Nucl. Eng. Des.* **2012**, *251*, 344–348. [[CrossRef](#)]
36. Osigwe, E.O.; Gad-Briggs, A.; Nikolaidis, T. Feasibility of a Helium Closed-Cycle Gas Turbine for UAV Propulsion. *Appl. Sci.* **2021**, *11*, 28. [[CrossRef](#)]
37. Alali, A.E.; Al-Shboul, K.F. Performance analysis of the closed Brayton power cycle in a small-scale pebble bed gas cooled reactor using different working fluids. *Ann. Nucl. Energy* **2018**, *121*, 316–323. [[CrossRef](#)]
38. Tesio, U.; Guelpa, E.; Verda, V. Multi-objective optimization of helium power cycle for thermo-chemical energy storage in concentrated solar power. *Energy Convers. Manag. X* **2021**, *12*, 100116. [[CrossRef](#)]

39. Gueymard, C. Prediction and Performance Assessment of Mean Hourly Global Radiation. *Sol. Energy* **2000**, *68*, 285–303. [CrossRef]
40. Gueymard, C.A.; Ruiz-Arias, J.A. Extensive worldwide validation and climate sensitivity analysis of direct irradiance predictions from 1-min global irradiance. *Sol. Energy* **2016**, *128*, 1–30. [CrossRef]
41. Mejdoul, R.; Taqi, M.; Ben, S.; Hassan, U.; Mohammedia, I.I. The Mean Hourly Global Radiation Prediction Models Investigation in Two Different Climate Regions in Morocco. *Int. J. Renew. Energy Res.* **2012**, *2*, 608–617.
42. Yao, W.; Li, Z.; Xiu, T.; Lu, Y.; Li, X. New decomposition models to estimate hourly global solar radiation from the daily value. *Sol. Energy* **2015**, *120*, 87–99. [CrossRef]
43. Power Data Access Viewer. 2020. Available online: <https://power.larc.nasa.gov/data-access-viewer/> (accessed on 1 March 2020).
44. Goswami, Y. *Principles of Solar Engineering*, 3rd ed.; CRC Press Taylor & Francis Group: Boca Raton, FL, USA, 2015.
45. Moreno-Gamboa, F.; Escudero-Atehortua, A.; Nieto-Londoño, C. Performance evaluation of external fired hybrid solar gas-turbine power plant in Colombia using energy and exergy methods. *Therm. Sci. Eng. Prog.* **2020**, *20*, 100679. [CrossRef]
46. Romero, M.; Buck, R.; Pacheco, J.E. An update on solar central receiver systems, projects, and technologies. *J. Sol. Energy Eng.* **2002**, *124*, 98–108. [CrossRef]
47. Duffie, J.; Beckman, W. *Solar Engineering of Thermal Processes*, 4th ed.; John Wiley & Sons: Hoboken, NJ, USA, 2013.
48. Chen, L.; Ni, N.; Sun, F. FTT Performance of a closed regenerative brayton cycle coupled to variable-temperature heat reservoir. In Proceedings of the International Conference on Marine Engineering, Varna, Bulgaria, 2–7 June 1996; pp. 371–1996.
49. Zhai, H.; Dai, Y.J.; Wu, J.Y.; Wang, R.Z. Energy and exergy analyses on a novel hybrid solar heating, cooling and power generation system for remote areas. *Appl. Energy* **2009**, *86*, 1395–1404. [CrossRef]
50. Zare, V.; Hasanzadeh, M. Energy and exergy analysis of a closed Brayton cycle-based combined cycle for solar power tower plants. *Energy Convers. Manag.* **2016**, *128*, 227–237. [CrossRef]
51. Atif, M.; Al-Sulaiman, F.A. Energy and exergy analyses of solar tower power plant driven supercritical carbon dioxide recompression cycles for six different locations. *Renew. Sustain. Energy Rev.* **2017**, *68*, 153–167. [CrossRef]
52. Yue, T.; Lior, N. Thermal hybrid power systems using multiple heat sources of different temperature: Thermodynamic analysis for Brayton cycles. *Energy* **2018**, *165*, 639–665. [CrossRef]
53. Petela, R. Exergy of undiluted thermal radiation. *Sol. Energy* **2003**, *74*, 469–488. [CrossRef]
54. Parrot, L.E. Theoretical upper limit to the conversion efficiency of solar energy. *Sol. Energy* **1978**, *21*, 227–229. [CrossRef]
55. Neises, T.; Turchi, C. A Comparison of Supercritical Carbon Dioxide Power Cycle Configurations with an Emphasis on CSP Applications. *Energy Procedia* **2014**, *49*, 1187–1196. [CrossRef]
56. Lee, H.J.; Kim, H.; Jang, C. Compatibility of Candidate Structural Materials in High-Temperature S-CO<sub>2</sub> Environment. In Proceedings of the 4th International Symposium—Supercritical CO<sub>2</sub> Power Cycles, Pittsburgh, PA, USA, 9–10 September 2014; pp. 1–9.
57. Ahn, Y.; Bae, S.J.; Kim, M.; Cho, S.K.; Baik, S.; Lee, J.I.; Cha, J.E. Review of supercritical CO<sub>2</sub> power cycle technology and current status of research and development. *Nucl. Eng. Technol.* **2015**, *47*, 647–661. [CrossRef]
58. Chai, L.; Tassou, S.A. A review of printed circuit heat exchangers for helium and supercritical CO<sub>2</sub> Brayton cycles. *Therm. Sci. Eng. Prog.* **2020**, *18*, 100543. [CrossRef]
59. CarbonDioxide—CoolProp 6.3.1dev Documentation. Available online: [http://www.coolprop.org/dev/fluid\\_properties/fluids/CarbonDioxide.html](http://www.coolprop.org/dev/fluid_properties/fluids/CarbonDioxide.html) (accessed on 21 March 2020).
60. Modelica Association. Modelica.Media.Air.DryAirNasa. Available online: <https://doc.modelica.org/Modelica%204.0.0/Resources/helpWSM/Modelica/Modelica.Media.Air.DryAirNasa.html> (accessed on 20 March 2021).
61. Helium—CoolProp 6.3.1dev Documentation. Available online: [http://www.coolprop.org/dev/fluid\\_properties/fluids/Helium.html](http://www.coolprop.org/dev/fluid_properties/fluids/Helium.html) (accessed on 21 March 2020).
62. Moreno-Gamboa, F.; Nieto-Londoño, C. Hybrid Brayton Multi-stage Concentrated Solar Power Plant Energy and Exergy Performance Study. *J. Energy Resour. Technol.* **2021**, *143*, 1–11. [CrossRef]
63. Ramírez-Cerpa, E.; Acosta-Coll, M.; Vélez-Zapata, J. Análisis de condiciones climatológicas de precipitaciones de corto plazo en zonas urbanas: Caso de estudio Barranquilla, Colombia. *Idesia* **2017**, *35*, 87–94. [CrossRef]
64. Kotas, T.J. *The Exergy Method of Thermal Plant Analysis*; Kreiger Publishing Company: Malabar, FL, USA, 1995.